Journal of Materials Chemistry A

ROYAL SOCIETY OF CHEMISTRY

PAPER

View Article Online
View Journal | View Issue

Open Access Article. Published on 04 March 2025. Downloaded on 5/10/2026 4:48:14 PM.
This article is licensed under a Creative Commons Attribution-NonCommercial 3.0 Unported Licence.

Check for updates

Cite this: J. Mater. Chem. A, 2025, 13, 9514

Rational design of hierarchical hollow-core dual-shell amorphous 3D nanospheres as an effective electrode material for hybrid supercapacitors†

Shaik Junied Arbaz, Bhimanaboina Ramulu and Jae Su Yu *

Received 6th January 2025
Accepted 14th February 2025

DOI: 10.1039/d5ta00108k

rsc.li/materials-a

Extensive research in energy storage has aimed to develop materials with exceptional morphological and electrochemical characteristics. In this report, we synthesized novel cobalt copper zinc (CCZ) nanospheres with a multilayered core–shell structure using a simple hydrothermal process, followed by low-temperature wet chemical synthesis. By optimizing the reaction time, we developed three-dimensional hierarchical CCZ nanospheres with a core–shell structure and hollow interior. The optimized CCZ-8 (8 h) hollow-core single-shell nanospheres exhibited an impressive areal capacity of 53.7 μA h cm^{-2} (29.8 mA h g^{-1}). To further enhance performance, the CCZ-8 material underwent wet chemical treatment using an ionic solution at low temperature, transforming it into Ni@CCZ-8 hollow-core dual-shell nanospheres. This modification significantly increased the areal capacity to 124.46 μA h cm^{-2} (76.06 mA h g^{-1}), with a cycling stability of 87.4% over 20 000 charge/discharge cycles. For validation, Ni@CCZ-8/Ni foam was used as a positive electrode in a pouch-type hybrid supercapacitor (HSC). The HSC achieved a peak energy density of 100.77 μW h cm^{-2} (25.58 W h kg^{-1}) and a maximum power density of 7500 μW h cm^{-2} (1923.07 W h kg^{-1}) with robust cycling stability. The HSC's performance was demonstrated by powering radio-remote-operated electronics and other real-time applications. This study not only advances nanomaterial-based energy storage devices but also highlights their practical potential in real-world applications.

1. Introduction

The demand for nature-friendly, renewable, and reliable energy resources has been steadily increasing due to the rapid increase in pollution levels associated with the eventual depletion of fossil fuels.[1] To overcome this deteriorating energy crisis, intense research is being carried out to discover alternative approaches for energy storage that can lessen the dependency on non-renewable resources.[2] Over the past few decades, supercapacitors (SCs) have attracted great attention as an appealing option for rechargeable energy-storage systems because of their high power density, extended endurance, and quick charge/discharge capabilities.[3–7] Several approaches have been adopted to create highly efficient and effective energy-storage electrode materials, including the architectural design of nanomaterials. The architectural design of nanomaterials refers to the morphological definition of the nanoparticles present in electrode materials. The shape, size, classification, and dimensions of nanoparticles may affect the reaction mechanism, electrochemical efficiency, and redox activity.[8,9]

Thus far, various morphological classifications have been reported for each material with corresponding unique merits. For instance, structures such as nanorods, nanowires, nanograss, nanohair, and nanopillars have one-dimensional (1D) morphologies with decreased diffusion resistance, increased ionic conductivity, and rapid charge transportation.[10–14] Meanwhile, 2D structures, such as nanosheets and nanoflakes, offer a high surface area that enhances the interaction area between the electrode and electrolyte.[15–18] Owing to these useful features, 2D materials are often preferred for attaining high redox performance. Furthermore, 3D nanostructures can present a large number of electroactive sites, accompanied by a high surface area for the electrolyte and material. These structures are known for their enhanced capabilities and vital roles in redox mechanisms.[19–21] 3D nanoparticles can be fabricated in a variety of shapes that vary widely depending on the surfactant and structure-directing agent. Core–shell-type nanoarchitectures have great potential in terms of energy storage and electrochemical kinetics. Core–shell-type nanostructures, as the name suggests, consist of a double-layer design in which one layer of the structure is covered entirely by another layer of nanostructure. The inner and outer layers are referred to as the core and shell, respectively. These core–shell-type morphologies

Department of Electronics and Information Convergence Engineering, Institute for Wearable Convergence Electronics, Kyung Hee University, 1732 Deogyeong-daero, Gihung-gu, Yongin-si, Gyeonggi-do 17104, Republic of Korea. E-mail: jsyu@khu.ac.kr

† Electronic supplementary information (ESI) available. See DOI: https://doi.org/10.1039/d5ta00108k

This journal is © The Royal Society of Chemistry 2025

Open Access Article. Published on 04 March 2025. Downloaded on 5/10/2026 4:48:14 PM.
This article is licensed under a Creative Commons Attribution-NonCommercial 3.0 Unported Licence.

enable the facile embedding of one material species into another, thus providing multiple functional advantages of nanoparticles.[22,23] Moreover, both layers can be made of the same geometry or different geometries that offer the merits of different morphologies.[24] Nevertheless, core–shell-type nanostructures integrate two different functional attributes within the same particle. This reason inspires many researchers to explore the specific classification of morphological designs.[22,25,26]

Furthermore, to boost the attributes and integrate additional features, hollow-type morphologies have been introduced in energy storage-based research. This design enables a hollow interior for the nanoparticles, thereby offering more space for redox activity. Owing to this feature, hollow-type core–shell nanostructures have been developed, which combine the advantages of both architectural constructs. The hollow interior serves as an individual reservoir by allowing the electrolyte to penetrate the deeper layers of the material. This mechanism may induce the wettability of the material, which makes it more hydrophilic.[27] Additionally, the voids in the hollow core provide extra space for charges and ions to accommodate, which can positively affect the charging and discharging of SCs.[28] These benefits could be further enhanced if multilayered core–shell-type materials could be designed with a hollow core.

Although a few past reports have claimed the usage of multilayered or core–shell-type architectures for electrochemical energy storage, a unique morphology containing three layers constructed of various nanoscaled morphologies along with a hollow core is rarely seen in the literature. This work reports the synthesis of multilayered 3D nickel (Ni)-coated cobalt copper zinc hollow-core dual-shell nanospheres (Ni@CCZ HCDSNSs) through a two-step fabrication technique. Initially, a bilayered architecture was acquired in the preparation of synthesized novel CCZ nanospheres that contained a hollow interior using a facile hydrothermal method involving various growth times (4, 8, and 12 h). The optimized CCZ-8 sample with 8 h of reaction time was further coated with Ni nanosheets using a simple wet chemical synthesis, thereby acquiring Ni@CCZ-8 material associated with three layers of nanostructures along with a hollow interior. The uniqueness of this material lies within the tactically designed morphology. The three layers of the Ni@CCZ-8 material acted as multilayered core–shell-type morphology in which the innermost layer served as hollow core and the rest of the two layers could be considered as shell layers. Furthermore, each layer of this architecture has evolved with a different morphology. Firstly, the innermost layer (core) is composed of minuscule nanoparticles that were agglomerated into a spherical shape with a hollow interior. The hollowness enables the encapsulation of electrolyte, thereby enhancing the surface interactions between the material and electrolyte. Furthermore, the hollowness also serves as the additional space for charge accommodation during electrochemical activity. The second layer (intermediate layer) is composed of 3D nanotube structures, providing the morphological merits of nanoscaled 3D morphology. Finally, the outermost layer contains nanoscaled 2D sheet-like structures that envelop the internal layers of the spheres. These 2D nanosheets provide additional surface area for the material–electrolyte interaction and also enhance the charge accommodation. Altogether, the Ni@CCZ-8 HCDSNSs draw their merits from different classifications of morphologies which include multilayered design, core–shell-type architecture, hollow-cored nanostructures, 2D nanosheets, and 3D nanocube structures. The material possessing such a complex morphology exhibited a good specific capacity and excellent stability after a long cycling process, which was enabled by the core–shell structure incorporating both Ni and Co as the active elements. In addition, a hybrid supercapacitor (HSC) fabricated with Ni@CCZ-8/Ni foam (NF) and activated carbon-coated NF (AC/NF) electrodes demonstrated promising real-time applications with acceptable energy and power densities.

2. Experimental section

A detailed description of the materials and chemicals used in this experiment is provided in the ESI.†

2.1. Synthesis of cobalt copper zinc (CCZ) hollow-core single-shell nanospheres (HCSSNSs)

To synthesize the transition metal-based HCSSNSs, cobalt acetate tetrahydrate ($Co(CH_3CO_2)_2 \cdot 4H_2O$) (50 mM) was added to 100 ml of ethylene glycol, followed by intense sonication and vigorous stirring. Once the cobalt acetate was completely dissolved into the solvent, copper acetate anhydrous ($Cu(CH_3CO_2)_2 \cdot H_2O$) (20 mM) was added to it, followed by the addition of zinc acetate dihydrate ($Zn(CH_3CO_2)_2 \cdot 2H_2O$) (30 mM). After obtaining a translucent mixture, 0.6 g of polyvinylpyrrolidone (PVP) was gradually added with vigorous stirring to prevent the formation of clumps. The entire solution was transferred to a liner and placed in an autoclave. The solvothermal experiment was performed for 8 h at 160 °C with a ramp rate of 5 °C min^{-1}. The post-experiment solution was centrifuged to separate the precipitate from the supernatant. The precipitate was cleaned several times with deionized water (DIW) several times and then with ethanol to eliminate traces of post-experimental solution. Later, the precipitate was dried in an oven at 70 °C for 24 to 48 h before pulverizing into a fine powder. This sample is denoted as CCZ-8. To optimize its electrochemical characteristics through a comparison and study of the impact of growth time on the nanostructures, two other samples were also synthesized using the aforementioned procedure, except for their reaction times (4 and 12 h). These materials were named CCZ-4 and CCZ-12, respectively.

2.2. Synthesis of HCDSNSs

Ionic deposition on the surface of the nanoparticles was performed to enhance the electrochemical characteristics of CCZ-8. Initially, the ionic solution was prepared by dissolving 5 mM of nickel nitrate hexahydrate ($Ni(NO_3)_2 \cdot 6H_2O$) into 50 ml of DIW. Then, 0.3 g of pre-synthesized CCZ-8 powder was added to the ionic solution under constant stirring. The solution was sonicated at regular intervals to separate the accumulated nanospheres. After a simultaneous stirring and sonication process

Open Access Article. Published on 04 March 2025. Downloaded on 5/10/2026 4:48:14 PM. This article is licensed under a Creative Commons Attribution-NonCommercial 3.0 Unported Licence.

was carried out for 10 to 15 min, the solution was transferred into a temperature-enduring glass beaker and placed in the oven for 2 h at 100 °C. The solution was centrifuged to collect the precipitate, which was washed with DIW and ethanol to remove undesired supernatant. The cleaned precipitate was then dried at 70 °C for 24 h. After pulverizing the dried sample, the obtained material was named Ni@CCZ-8.

3. Results and discussion

The synthesis and formation process of CCZ-8 HCSSNSs and Ni@CCZ-8 HCDSNSs are described in the schematic diagrams in Fig. 1. Initially, when $Co(CH_3CO_2)_2$ was added to ethylene glycol (EG) which is an organic solvent, the hydroxyl (OH^-) ions present in EG induce polarity that destabilized the ionic bonds of $Co(CH_3CO_2)_2$ and split the corresponding molecules into Co^{2+} and $CH_3CO_2^-$ ions that remained suspended in the solution. However, the acetate salt does not dissolve readily in EG because it is more viscous than other solvents such as water or ethanol. Nevertheless, upon vigorous stirring and sonication, the solution turned translucent with a scarlet tint, implying proper dissolution of the solute. $Cu(CH_3CO_2)_2$ was then gradually added to the solution under constant stirring and subjected to alternating stirring and sonication, followed by the addition of $Zn(CH_3CO_2)_2$ into the solution mixture. Once proper solvation of all the chemicals in the solvent was confirmed, the solution mixture was stirred rapidly, and PVP was steadily added to prevent clumping. PVP is a polymer with long chains that interact and form complex hydrogen bonds with the OH^- ions, resulting in its solubility. During the solvothermal process, the mixed solution began to absorb the thermal energy provided by the autoclave instrument in the form of heat. Simultaneously, freely suspended metal ions from the dispersed/dissolved salts accumulated under the influence of PVP. In this case, PVP in the presence of the organic solvent, EG, might serve as an ionic binder by accumulating metal ions in the nanoscale particles. As the experiment was carried out for 8 h, the morphology could evolve concerning the ongoing experiment at a high temperature of 180 °C. The formation of two layers within the first step of the experimental process could be explained with the help of the phenomenon of Ostwald's ripening process that takes place with respect to the growth time. During the initial stages of the experiment, basic single-layered nanospheres might be developed due to the agglomeration of the freely suspending metal ions, influenced by Ostwald's ripening process. At this point in the presence of PVP

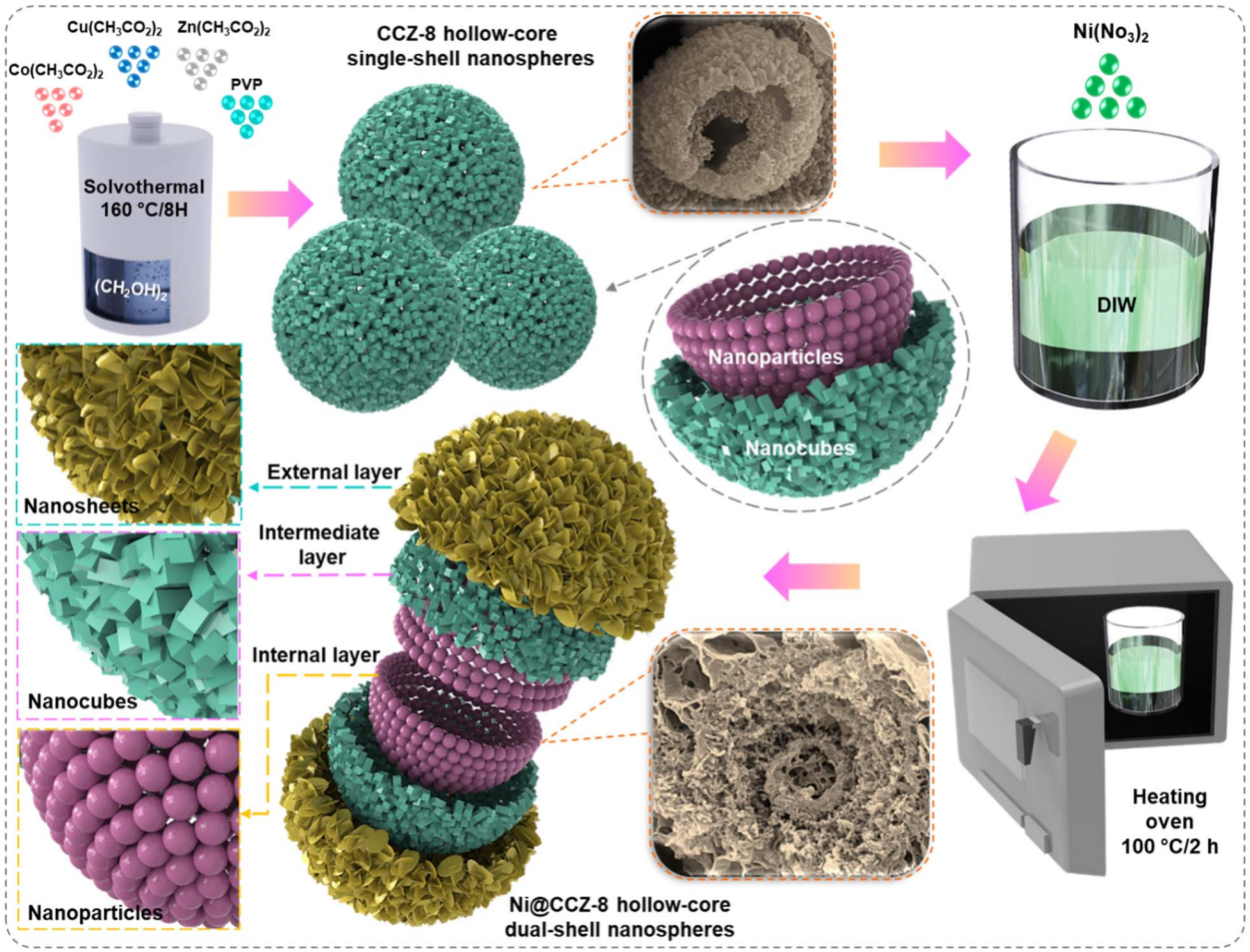

Fig. 1 Schematic diagrams illustrating the preparation of CCZ-8 HCSSNSs and Ni@CCZ-8 HCDSNSs.

 This journal is © The Royal Society of Chemistry 2025

Open Access Article. Published on 04 March 2025. Downloaded on 5/10/2026 4:48:14 PM.
This article is licensed under a Creative Commons Attribution-NonCommercial 3.0 Unported Licence.

molecules in the organic medium, the experiment continued enabling the agglomeration of the metal ions around the already existing nanospheres, thus promoting the formation of another layer over its surface. Due to the availability of enough time and under a constant temperature of 160 °C, the second layer might have a chance to be developed into nanocubed structures. Owing to the reaction time governing the evolution of the CCZ-8 nanoparticles, it could result in the formation of two-layered nanospheres of the material as indicated in the schematics. Later, in the wet chemical synthesis, when the $Ni(No_3)_2 \cdot 6H_2O$ was added into DIW, the nickel salt rapidly dissolved into the DIW owing to the solvent's high polarity, thereby splitting into Ni^{2+} and NO_3^- ions that freely suspend within the solution. As soon as the dried CCZ-8 powder was introduced, Ni^{2+} ions started to accumulate on the surface of the CCZ-8 nanospheres. When placed in an oven, the solution provides sufficient thermal energy for further reactions to take place. During this reaction, Ni^{2+} ions began to adhere to the surface of the CCZ-8 nanospheres, and under the influence of heat, these ions agglomerated radially, forming 2D nanosheets. The evolution of these nanosheets on the CCZ-8 HCSSNSs resulted in the formation of a secondary shell-like layer. These dual-shell Ni@CCZ-8 nanospheres have hollow interiors with three layers consisting of different nanomorphologies. The first and most interior layers were composed of tiny nanoparticles, the second intermediate layer was composed of nanocubes, and the outermost third layer was composed of nanosheets, which provided the Ni@CCZ-8 material with the merits of multiple morphologies, as shown in the schematic diagrams.

The surface morphologies and architectures of the synthesized samples were determined by using a field-emission scanning electron microscope (FE-SEM). Fig. 2(a)(i) shows the FE-SEM images of the CCZ-8 particles at low magnification. This indicated a cluster of multiple nanospheres in the aforementioned sample. At high magnification (Fig. 2(a)(ii)), a layer made of nanocubes surrounded an internal core consisting of tiny nanoparticles. Moreover, the core is hollow from the interior. To examine the elemental presence and elemental distribution in the CCZ-8 sample, energy-dispersive X-ray spectroscopy (EDS) and elemental mapping techniques were used as shown in Fig. S1 of the ESI.† As the inner layer (core) and outer layer (shell) of the CCZ-8 material are inevitably formed during the first step of the synthesis process, it is not possible to completely separate both layers and then verify them individually for EDS and elemental mapping. However, the EDS analysis and elemental mappings were measured on the surface of the CCZ-8 nanosphere consisting of an opening, thus disclosing the inner layer (core). The resultant EDS spectrum in Fig. S1(a) of the ESI† displayed the existence of Co, Cu, C, Zn, O, and N elements, and through the elemental mapping images in Fig. S1(b)(i–vi) of the ESI,† it is revealed that there is a homogeneous presence of Co, Cu, C, Zn, O, and N elements in the core and the shell layers of CCZ-8 particles. The morphology of the CCZ-4 sample is presented in Fig. S2(a) of the ESI.† The low-magnification image of the sample shown in Fig. S2(a)(i) of the ESI† showed the clustered particles. The sizes of the spheres are identical to those of the CCZ-8 sample. Magnified images in Fig. S2(a)(ii) of the ESI† revealed that the spheres were hollow from the inside and had not yet developed a second outer layer.

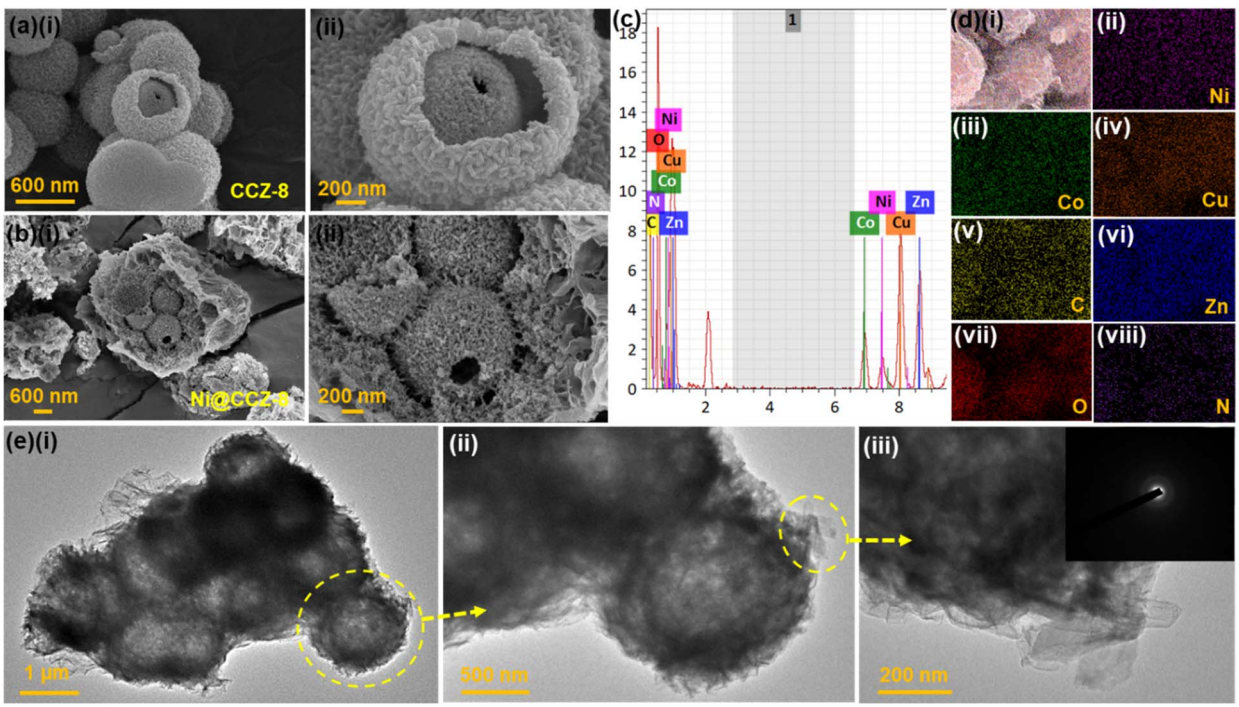

Fig. 2 (a) (i–iii) FE-SEM images of the CCZ-8 material and (b) (i, ii) FE-SEM images of the Ni@CCZ-8 material. (c) EDS spectrum, (d) (i–viii) elemental mapping images, and (e) (i–iii) TEM images of the Ni@CCZ-8 HCDSNSs, including the corresponding SAED pattern in the inset.

Open Access Article. Published on 04 March 2025. Downloaded on 5/10/2026 4:48:14 PM.
This article is licensed under a Creative Commons Attribution-NonCommercial 3.0 Unported Licence.

Highly magnified images shown in Fig. S2(a)(iii) of ESI† showed the absence of a layer composed of nanocubes on the spheres, implying an underdeveloped external surface. The particles did not undergo complete development considering the short reaction times during the experimental process. The particles of CCZ-12 are shown in Fig. S2(b) of the ESI.† The low-magnification FE-SEM image in Fig. S2(b)(i) of the ESI† showed the accumulated CCZ-12 spheres. In the high-magnification FE-SEM images in Fig. 2(b)(ii) and S2(b)(iii) of the ESI,† it was observed that the exterior layer was entirely composed of the nanocubes. Because of the extended reaction time, these particles attained much tougher layers than their predecessors. Fig. 2(b)(i) shows a low-magnification FE-SEM image of the Ni@CCZ-8 sample, which consists of accumulated nanospheres covered in nanosheets. At high magnification (Fig. 2(b)(ii)), the nanospheres were covered and embedded in the layers of the nanosheets, resulting in a multilayered architecture. Fig. 2(c) shows the EDS spectrum of Ni@CCZ-8. The spectrum confirmed the presence of Ni, Co, Cu, C, Zn, O, and N. The overlay image and corresponding elemental mappings (Fig. 2(d)(i–viii)) confirm the presence of these elements in the sample. The internal architecture of the Ni@CCZ-8 HCDSNSs was examined by transmission electron microscope (TEM) analysis. Fig. 2(e)(i) shows the low-magnification TEM images of the accumulated Ni@CCZ-8 particles. At high magnification (Fig. 2(e)(ii)), the spheres were composed of multiple layers with hollow interiors. In the high-magnification TEM images in Fig. 2(e)(iii), a layer of porous nanosheets was observed to surround the surface of the nanospheres. The inset in Fig. 2(e)(iii) shows the selected area electron diffraction (SAED) pattern. This did not contain any patterns owing to the lack of well-defined grain boundaries, indicating the amorphous nature of the material.

Surface characterization was performed on the Ni@CCZ-8 material to obtain further information. X-ray diffraction (XRD) analysis was performed to examine the phases of the

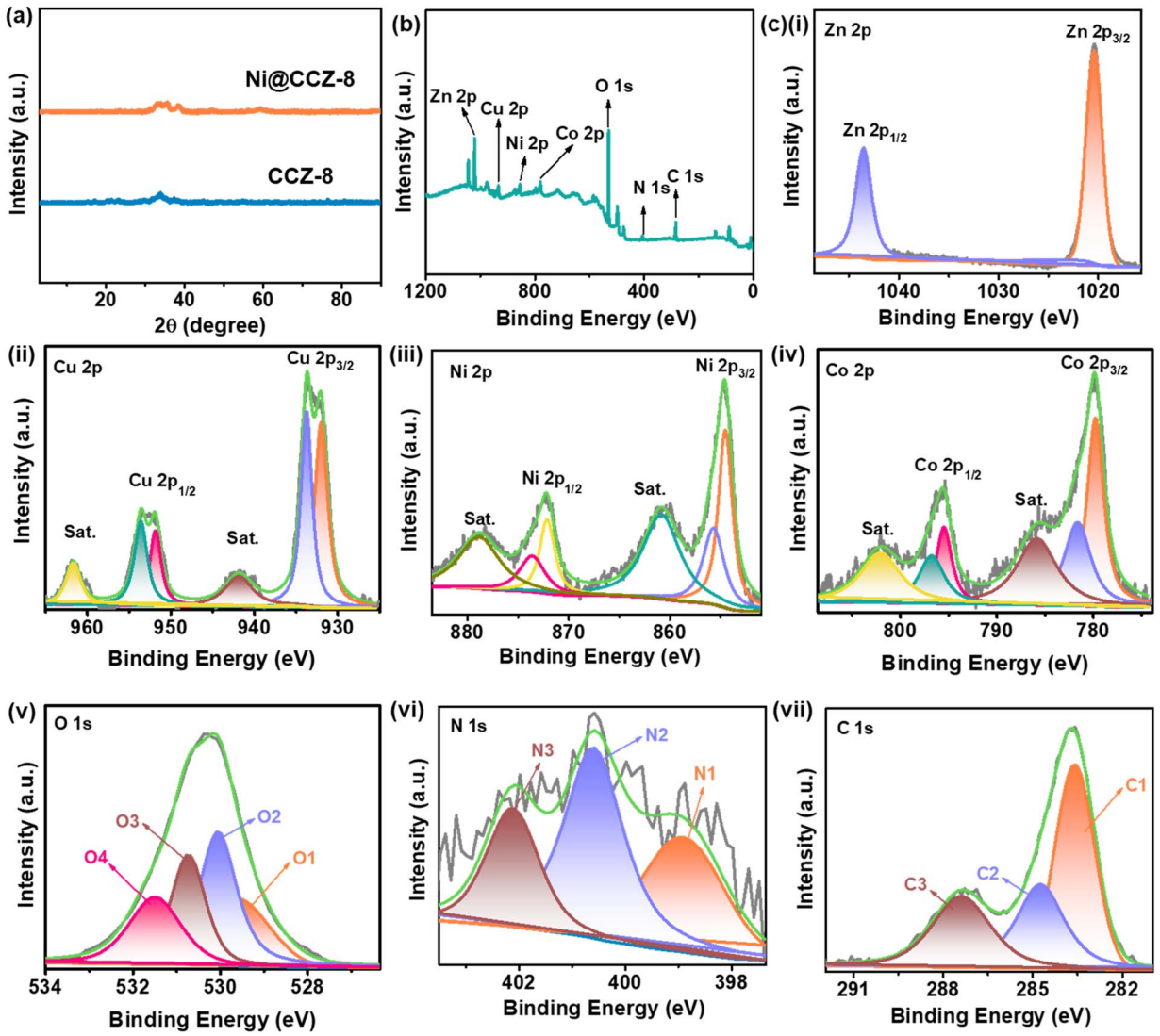

Fig. 3 (a) XRD patterns of the CCZ-8 and Ni@CCZ-8 materials, (b) XPS survey scan spectrum of the Ni@CCZ-8 material, and (c) (i–vii) high-resolution XPS core-level spectra of Zn 2p, Cu 2p, Ni 2p, Co 2p, O 1s, N 1s and C 1s for the Ni@CCZ-8 material.

 This journal is © The Royal Society of Chemistry 2025

Open Access Article. Published on 04 March 2025. Downloaded on 5/10/2026 4:48:14 PM. This article is licensed under a Creative Commons Attribution-NonCommercial 3.0 Unported Licence.

synthesized materials. As shown in Fig. 3(a), neither CCZ-8 nor Ni@CCZ-8 exhibited any significant high-intensity peaks, implying the amorphous nature of the material. The XRD result supports the SAED result and explains the absence of a definite circular pattern. The Ni@CCZ-8 material was subjected to X-ray photoelectron spectroscopy (XPS) to determine the surface oxidation and valence states of the existing elements. A complete survey scan in Fig. 3(b) presents the spectrum with the peaks arising at the binding energies of 1020.44, 933.44, 854.68, 779.97, 530.31, 398.55, and 283.73 eV that correspond to the Zn 2p, Cu 2p, Ni 2p, Co 2p, O 1s, N 1s, and C 1s, respectively. The high-resolution XPS spectra of the core elements are shown in Fig. 3(c)(i)–(vii), where each peak was fitted using the 'Lorentzian–Gaussian' fitting technique. The peaks in the Zn 2p spectrum (Fig. 3(c)(i)) could be seen at 1020.41 and 1043.49 eV, which represent the corresponding characteristics of Zn $2p_{3/2}$ and Zn $2p_{1/2}$, respectively. The presence of these characteristic peaks confirmed the existence of the Zn^{2+} oxidation state.[29] The Cu 2p core-level spectrum shown in Fig. 3(c)(ii) had two main peaks at 933.15 and 953.28 eV corresponding to the Cu $2p_{3/2}$ and Cu $2p_{1/2}$, respectively, that correspond to the presence of Cu/Cu^{+} and Cu^{2+} oxidation states. The associate satellite peaks were fitted at the binding energies of 941.08 and 961.17 eV.[30] The Ni 2p spectrum in Fig. 3(c)(iii) showed two unique peaks, Ni $2p_{3/2}$ at 854.57 eV and Ni $2p_{1/2}$ at 872.20 eV, with each characteristic peak containing a set of doublet peaks attributing to the Ni^{2+} and Ni^{3+} valency states of Ni. The corresponding satellite peaks merging at 860.82 and 878.76 eV could be observed.[31] The Co 2p spectrum is shown in Fig. 3(c)(iv), where the typical peaks are present at 779.86 eV (Co $2p_{3/2}$) and 795.55 eV (Co $2p_{1/2}$) along with their satellite peaks at 785.87 and 802.11 eV.[32] The core-level O 1s spectra in Fig. 3(c)(v) had four peak fittings. The peak at 529.51 eV (O1) indicates the metal–oxygen bond (M–O), while the peak at 530.04 eV (O2) represents low oxygen coordination and a defective lattice. The peak at the binding energy of 530.74 eV (O3) specifies chemically/physically adsorbed water molecules. The peak at a binding energy of 531.48 eV (O4) represents the oxygen bonds (O=C).[33,34] The core-level spectra of N 1s in Fig. 3(c)(vi) exhibited three fitted peaks. The peak at 398.91 eV (N1) shows pyrrolic nitrogen, the peak at 400.6 eV (N2) represents graphitic nitrogen, and the peak at 402.11 eV displays nitrogen and oxygen bonds (N–O).[35] The core-level spectra of C 1s in Fig. 3(c)(vii) were fitted with three peaks. Peak C1 (283.59 eV is associated with the sp^2 hybridization of carbon atoms, resulting in (C–C) bonds. Peak C2 (284.72 eV represents the sp^3 hybridization between the double bonds (C=C) of carbon atoms. The peak C3 emerging at 287.36 eV implies the bonds between the carbon and oxygen atoms (C–O/C=O).[36]

All the fabricated materials contain more than one layer in their corresponding morphology. Hence, to examine the surface area of the CCZ-4, CCZ-8, CCZ-12, and Ni@CCZ-8 samples, they were subjected to the Brunauer–Emmett–Teller (BET) measurement. Following that, to determine the pore diameter and pore size distribution, Barrett–Joyner–Halenda (BJH) analysis was carried out on the same samples. The BET and BJH measurements were conducted at a cryogenic temperature (77 K) that was successfully achieved using liquid nitrogen. The samples were pretreated at 90 °C for about 120 min in the presence of a vacuum to eliminate any undesired moisture or adsorbed water molecules from the material. Later, all the sample powders were subjected to the testing process. The BET analysis evaluates the specific surface area of the material, which determines the magnitude of material and electrolyte interaction. The details regarding the specific surface area also disclose the ability of the material to enable the charge accommodation during redox reactions. On the other hand, the BJH results specify the additional details concerning the pore structure existing in the nanoparticles from each sample. The analysis results of the CCZ-4, CCZ-8, CCZ-12, and Ni@CCZ-8 samples are given in Fig. S3 of the ESI.† The adsorption/desorption isotherm of the CCZ-4 sample in Fig. S3(a)(i) of the ESI† exhibited a type-II(b) associated with the 'H3' hysteresis desorption curve. The type-II isotherms imply the presence of a mesoporous system with weak and strong interactions between the adsorbate (CCZ-4) and adsorbent (N_2). The type-II isotherm contains knee point 'B' as seen in the corresponding plot, which indicates a monolayer formation accompanied by the increase in the gas pressure. The 'H3' hysteresis loop indicates the irreversible capillary condensation that took place within the mesopores during the desorption process. As per the BET analysis, the specific surface area (a_s) of the CCZ-4 sample is 11.884 $m^2\ g^{-1}$. From the BJH plot of the corresponding sample in Fig. S3(a)(ii) of the ESI,† the CCZ-4 material contains a minimum number of micropores with an average number of mesopores extending between 5 and 80 nm. Furthermore, it is noted that the average pore diameter (d_p) is 16.596 nm with a pore volume (V_p) of 0.081553 $cm^3\ g^{-1}$. Similarly, the CCZ-8 sample displayed a type-II isotherm curve with minimal capillary condensation as seen in Fig. S3(b)(i) of the ESI.† This implies the presence of a mesopore-dominant mixed pore system as seen in the BJH plot (Fig. S3(b)(ii) of the ESI†). Furthermore, an inflection point 'B' represents the monolayer formation. The CCZ-8 sample has a specific surface area of 21.087 $m^2\ g^{-1}$ along with a pore volume of 0.117 $cm^3\ g^{-1}$ and an average pore size of 13.346 nm. The adsorption–desorption isotherm analysis results of the CCZ-12 sample in Fig. S3(c)(i) of the ESI† represented a type-II(b) isotherm plot with an 'H4' hysteresis loop, thus indicating aggregated slit-like pores in the sample. Moreover, it also indicates the considerable level of irreversible capillary condensate during the desorption process. A minor knee point 'B' at the start of the adsorption curve represents monolayer formation of the gas. In the BJH plot in Fig. S3(c)(ii) of the ESI,† the CCZ-12 material contains a mixed porous system of micropores and mesopores and also small quantities of macropores. The specific surface area of the CCZ-12 sample is noted to be 18.645 $m^2\ g^{-1}$ along with an average pore diameter of 11.754 nm and a pore volume of 0.086019 $cm^3\ g^{-1}$. Here, it could be seen that among the three CCZ samples, the CCZ-8 material demonstrated a high pore volume with an increased surface area that can enable the CCZ-8 material to contribute with an optimized electrochemcial performance during redox activity, compared to those of the CCZ-4 and CCZ-12 materials. Finally, the adsorption and desorption isotherm graph of the Ni@CCZ-8 sample (Fig. S3(d)(i) of the ESI†)

Open Access Article. Published on 04 March 2025. Downloaded on 5/10/2026 4:48:14 PM. This article is licensed under a Creative Commons Attribution-NonCommercial 3.0 Unported Licence.

disclosed a type-II(b) with 'H3' hysteresis loop. The hysteresis loop is formed due to the capillary condensate within micropores. This sample also indicates a knee point 'B' at the initial point of the adsorption curve. The BJH plot in Fig. S3(d)(ii) of the ESI† showed that this sample contains pores ranging between 2–100 nm, thus forming a mixed pore system. The specific surface area of the Ni@CCZ-8 material is 101.71 $m^2 g^{-1}$ while the average pore diameter is 14.539 nm with a pore volume of 0.3534 $cm^3 g^{-1}$. Due to a superior surface area of 101.71 $m^2 g^{-1}$ and pore volume of 0.3534 $cm^3 g^{-1}$, the Ni@CCZ-8 HCDSNSs would be able to offer an enhanced charge accommodation and ion intercalation. The BET/BJH details corresponding to the CCZ-4, CCZ-8, CCZ-12, and Ni@CCZ-8 samples are given in Table 1.

To determine the electrochemical response of all the synthesized materials, they were coated onto NF, which served as the current-collecting substrate. A detailed description of electrode fabrication is provided in the ESI.† The electrodes fabricated from CCZ-4, CCZ-8, CCZ-12, and Ni@CCZ-8 were named CCZ-4/NF, CCZ-8/NF, CCZ-12/NF, and Ni@CCZ-8/NF electrodes, respectively. The comparative CV profiles of CCZ-4/NF, CCZ-8/NF, and CCZ-12/NF electrodes are presented in Fig. S4(a) of the ESI.† The CV curves were analyzed at a scan rate of 15 mV s^{-1} under a fixed potential window of 0–0.55 V. These curves revealed that the CCZ-8/NF electrode displayed higher redox activity than the other two electrodes. This is attributed to the contributions of both the core and shell layers of the CCZ-8 material. In contrast, the CCZ-4/NF electrode showed reduced electrochemical activity owing to the presence of underdeveloped CCZ-4 nanospheres. The CCZ-12/NF electrode exhibited almost the same redox response as the CCZ-8/NF electrode, but slightly less, as the overgrowth of the CCZ-12 nanospheres resulted in toughening of the external and internal layers, leading to a reduction in the impregnation process during redox reactions. Moreover, the area under the reduction and oxidation peaks was smaller than that of the CCZ-8/NF electrode, indicating the superiority of the latter. The comparative GCD profiles of the three electrodes are shown in Fig. S4(b) of the ESI.† The GCD curves were measured at a current density of 3 mA cm^{-2} in the potential window of 0–0.55 V. Here, the CCZ-8/NF electrode showed a higher performance than the other two electrodes owing to the morphological construction of the corresponding nanospheres. The CCZ-8 material contains hollow core–shell-type nanospheres that offer ample space to accommodate charges during the charging process. Moreover, the hollow interior allows the electrolyte to diffuse within the structure, thereby enhancing the interactions between the active material and the electrolyte. The external layer of the CCZ-8 HCSSNSs was composed of nanocubes, and this rough surface effectively increased the surface area, enhancing electrochemical activity. In contrast, the CCZ-4/NF electrode exhibited a low discharge response owing to the presence of a single layer and underdeveloped CCZ-4 nanospheres. The absence of a shell layer and a rough surface in the existing layer may reduce the effective surface area, which can decrease charge accommodation. In contrast, the CCZ-12 particles from the CCZ-12/NF electrode contained overdeveloped nanospheres that prevented the charges/ions from accessing the hollow interior of the nanostructures. Based on the comparative GCD profiles, the corresponding areal capacity values were calculated using eqn. (S1) of the ESI (Fig. S4(c) of the ESI).† The CCZ-8/NF electrode demonstrated the highest areal capacitance of 51.5 μA h cm^{-2} at 3 mA cm^{-2}, while the CCZ-4/NF and CCZ-12/NF electrodes exhibited the areal capacities of 20.1 μA h cm^{-2} and 44.8 μA h cm^{-2}, respectively. From the investigation of the CCZ-4, CCZ-8, and CCZ-12 samples, it is noticed that there is a strong impact of the growth time on the development of the nanospheres. The CCZ-4 material contains nanospheres that are underdeveloped with only a single layer with a smooth surface that might reduce the effective surface area. The CCZ-8 nanospheres had two layers with the external layer made of notably thinner and smaller nanocubes, making it thin enough to enable electrolyte soaking and encapsulation. However, the CCZ-12 material contained nanospheres that were allowed to develop over 12 h of reaction time. This resulted in an external layer constructed of comparatively larger nanocubes with comparatively thick outer walls. Probably, this could prevent easy electrolyte interactions with the internals of the nanospheres, thus preventing the material from achieving its maximum electrochemical performance. The electrochemical properties of the CCZ-4/NF electrode are presented in Fig. S5 of the ESI.† The CV test of this electrode was analyzed under various scan rates, differing from 5–30 mV s^{-1} under a fixed potential window of 0–0.55 V. All the curves displayed oxidation and reduction peaks that signify reversible redox reactions. The area under the CV curve is proportional to the scan rate. The GCD profiles of the electrodes are presented in Fig. S5(b) of the ESI.† These nonlinear charge/discharge curves imply that the material is faradaic-type and can undergo redox activity. The corresponding areal capacities (Fig. S5(c) of the ESI†) were calculated using eqn (S1) of the ESI.† The CCZ-4/NF electrode demonstrated an areal capacity of 37.2 μA h cm^{-2} (21.69 mA h g^{-1}), at an initial current density of 1 mA cm^{-2}. The electrochemical characteristics of the CCZ-8/NF electrode are

Table 1 BET/BJH analysis results of the CCZ-4, CCZ-8, CCZ-12, and Ni@CCZ-8 materials

Sample name	Isotherm type	Specific surface area (a_s)	Average pore diameter (d_p)	Pore volume (V_p)
CCZ-4	Type-II(b)/H3	11.884 $m^2 g^{-1}$	16.596 nm	0.081 $cm^3 g^{-1}$
CCZ-8	Type-II/minimal condensate	21.087 $m^2 g^{-1}$	13.346 nm	0.117 $cm^3 g^{-1}$
CCZ-12	Type-II(b)/H4	18.645 $m^2 g^{-1}$	11.754 nm	0.086 $cm^3 g^{-1}$
Ni@CCZ-8	Type-II(b)/H3	101.71 $m^2 g^{-1}$	14.539 nm	0.353 $cm^3 g^{-1}$

 This journal is © The Royal Society of Chemistry 2025

Open Access Article. Published on 04 March 2025. Downloaded on 5/10/2026 4:48:14 PM. This article is licensed under a Creative Commons Attribution-NonCommercial 3.0 Unported Licence.

shown in Fig. S6 of the ESI.† The CV voltammograms of the CCZ-8/NF electrode are shown in Fig. S6(a) of the ESI† at scan rates of 5–30 mV s^{-1} in the potential window of 0–0.55 V. The CV curves exhibited redox peaks with magnitudes that followed the increasing scan rates. The CV curves were proportional to the scan rate, indicating good redox reversibility and electrochemical activity. Moreover, at every scan rate, a significant increase in the area under the oxidation and reduction peaks was observed. The GCD profiles of the electrode are shown in Fig. S6(b) of the ESI† at different current densities varying from 1 to 10 mA cm^{-2} within the potential window of 0–0.55 V. Similar to the previous electrode, the GCD curves were non-linear, suggesting a faradaic-type material. The areal capacity of the electrodes was calculated based on the corresponding GCD profile. The maximum areal capacity of the CCZ-8/NF electrode was 53.7 μA h cm^{-2} (29.83 mA h g^{-1}) at 1 mA cm^{-2}. The CV curves, GCD curves, and areal capacity values of the CCZ-12/NF electrode are shown in Fig. S7 of the ESI.† The CV curves (Fig. S7(a) of the ESI†) were analyzed in the potential window of 0–0.55 V at scan rates of 5–30 mV s^{-1}. All the CV curves indicated redox reactions with good reversibility in proportion to varying scan rates. As the scan rate reached beyond 20 mV s^{-1}, a slight deformation in the CV curve could be noticed, which is accompanied by an observable reduction of redox area under the peaks. At higher scan rates, the curves exhibited a narrower shape, indicating a gradual disturbance in the redox activity. Fig. S7(b) of the ESI† shows various GCD curves that were analyzed under the fixed potential window of 0–0.55 at 1–30 mA cm^{-2}. Similar to the previous electrodes, faradaic behavior was observed for this working electrode. The associated areal capacities are presented in Fig. S7(c) of the ESI.† At 1 mA cm^{-2}, the CCZ-12/NF electrode revealed an areal capacity of 47.3 μA h cm^{-2} (26.31 mA h g^{-1}). To further enhance the electrochemical properties of CCZ-8, it was decorated with Ni nanosheets enveloping the nanospheres. This resulted in the synthesis of trilayered Ni@CCZ-8 HCDSNSs with a unique morphology. The outer, middle, and internal layers were composed of Ni nanosheets, CCZ nanocubes, and CCZ nanoparticles, respectively. Ni@CCZ-8 was coated onto the surface of the NF to obtain a Ni@CCZ-8/NF electrode. Comparative CV voltammograms of the CCZ-8/NF and Ni@CCZ-8/NF electrodes are shown in Fig. 4(a). Even at the same scan rate of 15 mV s^{-1}, the Ni@CCZ-8/NF electrode showed a higher current response compared to the CCZ-8/NF. This superior performance can be attributed to the presence of Ni nanosheets. Ni is known to provide a high redox response, and porous nanosheets provide an additional active surface area. The comparative GCD profiles of the CCZ-8/NF and Ni@CCZ-8/NF electrodes at a fixed current density of 3 mA cm^{-2} are shown in Fig. 4(c). Similar to the CV profile, the GCD profile indicated that Ni@CCZ-8 had a longer discharge time than CCZ-8. The additional layer made of Ni sheets effectively increased the specific surface area of the material which enabled an increased number of charges to be accommodated during the charge/discharge process, further boosting its performance. Furthermore, the large pore volume offered a high ion diffusion into the internal layers of the nanoarchitecture. The comparative areal capacities based on the GCD profiles are shown in Fig. 4(c). It was observed that the areal capacity of the CCZ-8/NF electrode was 51.5 μA h cm^{-2}, but the Ni@CCZ-8/NF electrode exhibited an areal capacity of 123.36 μA h cm^{-2}. Electrochemical comparisons of the CCZ-4/NF, CCZ-8/NF, and CCZ-12/NF electrodes and their electrochemical characteristics are provided in ESI.† The CV curves of the Ni@CCZ-8/NF electrode (Fig. 4(d)) are displayed at different scan rates of 5–30 mV s^{-1} within a fixed potential window of 0–0.55 V. All the CV curves contain the redox peaks indicating electrochemical activity during the measurement. The increasing area under each CV curve also implies proportional electrochemical kinetics of the material corresponding to the increasing scan rate. The GCD profiles of the same electrode are shown in Fig. 4(e) in the potential window of 0–0.55 V at 2–10 mA cm^{-2}. The non-linear or non-triangular GCD curves imply the faradaic-type behavior of the material during the electrochemical tests. At the initial current densities, the eventual change in the potential with respect to the discharge time (dV/dt) resulted in the appearance of a discharge plateau that signified the ongoing diffusion of ions/charges during redox activity. Based on the GCD profiles, the areal capacity was calculated using eqn (S1) of the ESI† (Fig. 4(f)). For an active electrode area of 1 × 1 cm^{-2}, the maximum areal capacity of the Ni@CCZ-8/NF electrode was 124.5 μA h cm^{-2} at 2 mA cm^{-2}. For a mass loading of 2 mg of material, the maximum specific capacity of Ni@CCZ-8/NF electrode at a specific current density of 1 A g^{-1} was 76.06 mA h g^{-1} as shown in Fig. S8 of the ESI.† The performance of the Ni@CCZ-8/NF electrode in terms of areal capacity was compared to the performances from previous literature and are represented in Table 2. During the redox operation in the electrode material, the charge storage is governed by the combination of faradaic reactions that result in the diffusion-controlled process and non-faradaic reactions that lead to surface controlled charge-storing process. To investigate the corresponding contribution of the faradaic and non-faradaic processes, the CV profile of the Ni@CCZ/NF electrode was analyzed in association with the following power law:

$$i = av^b$$

The above equation indicates the power law that defines the relationship between the resultant current response to the contribution of componential faradaic and non-faradaic currents at a particular scan rate of the CV curve. In the power law equation, the variables i and ν represent the current (A) and the scan rate (V s^{-1}), respectively, while the parameters a and b determine if the charge storage mechanism is either a faradaic process or a non-faradaic process. Specifically, the parameter b signifies whether the storage process is purely diffusion-controlled or purely surface-based, or a proportional combination of both processes. If the value of b is 0.5, then it is a diffusion-dominant storage mechanism and if the value of b is 1, it implies a purely surface-based capacitive-type storage mechanism. If the parameter b bears a value somewhere between 0.5 and 1, then it indicates a combined contribution from both the storing mechanisms. Fig. S9(a) of the ESI† shows

Open Access Article. Published on 04 March 2025. Downloaded on 5/10/2026 4:48:14 PM.
This article is licensed under a Creative Commons Attribution-NonCommercial 3.0 Unported Licence.

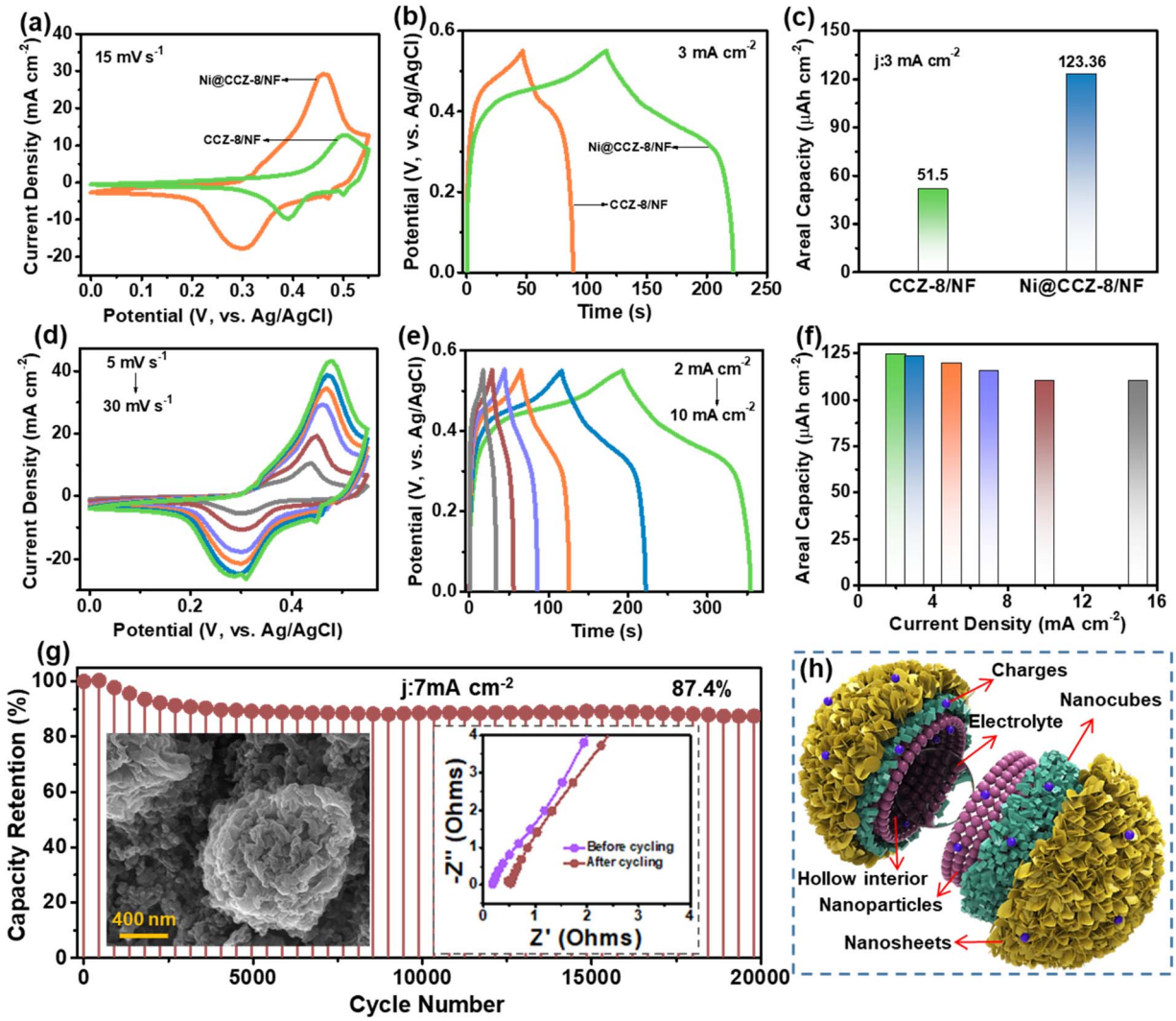

Fig. 4 Comparative (a) CV curves, (b) GCD curves, and (c) areal capacity values of the CCZ-8/NF and Ni@CCZ-8/NF electrodes. (d) CV profiles, (e) GCD profiles, and (f) areal capacity values of the Ni@CCZ-8/NF electrode. (g) Cycling test result and comparative EIS plots before and after the cycling test for the Ni@CCZ-8/NF electrode. (h) Exploded schematic view of the Ni@CCZ-8 HCDSNSs. The inset of (g) shows the FE-SEM image of the Ni@CCZ-8/NF electrode after the cycling test.

that the corresponding b value is acquired by analyzing the slope of the linear graph that was plotted between $\log(i)$ and $\log(v)$. From the analysis, the Ni@CCZ-8/NF electrode obtained a b value of 0.7, thus implying the existence of a diffusion-controlled mechanism in association with the capacitive-type surface-controlled mechanism.[37] Fig. S9(b) of the ESI† represents the current contribution in the Ni@CCZ-8 material at various scan rates. It is observed that the diffusion-type mechanism is dominant at lower scan rates. Nevertheless, following the ascending scan rate, the charge storage process tends to be

Table 2 Areal capacity comparison of the Ni@CCZ-8/NF electrode with previously published electrode materials

Active material	Synthesis method	Electrolyte	Areal capacity (μA h cm^2)	Ref.
$MnCo_2O_{4.5}$@δ-MnO_2	Wet-chemical synthesis	1 M Na_2SO_4	119.1 μA h cm^{-2}	38
$Co_3S_4/CuS_2/NiS_2$	Prussian-blue analogue technique	1 M KOH	70.3 mA h g^{-1}	39
Bi_2S_3@g-C_3N_4	Hydrothermal	1 M KOH	41.53 μA h cm^{-2}	21
Manganese oxide films (Ni foil)	Electrodeposition	0.1 M Na_2SO_4	18.1 μA h cm^{-2}	40
MnO_2@Ppy	Water bath	1 M Na_2SO_4	46 μA h cm^{-2}	41
$NiCo_2O_4$ nanorods	Solvothermal method	2 M KOH	29.1 μA h cm^{-2}	42
Co_3O_4@$NiCo_2O_4$ core–shell arrays	Hydrothermal method	2 M KOH	59.7 μA h cm^{-2}	43
Ni@CCZ-8 HCDSNSs	Hydrothermal method	2 M KOH	124.46 μA h cm^{-2}	This work

 This journal is © The Royal Society of Chemistry 2025

Open Access Article. Published on 04 March 2025. Downloaded on 5/10/2026 4:48:14 PM.
This article is licensed under a Creative Commons Attribution-NonCommercial 3.0 Unported Licence.

dominated by the surface-based process. The cycling test (Fig. 4(g)) was carried out to investigate the endurance of the material over a long cycling span for 20 000 charge/discharge cycles at 7 mA cm^{-2}. Even after 20 000 cycles, the material retained 87.4% of its initial capacity retention. The FE-SEM image in the inset of Fig. 4(g) displayed the Ni@CCZ-8 nanosphere from the Ni@CCZ-8/NF electrode after the cycling test. By observing the FE-SEM image, it is deduced that the nanospheres from the Ni@CCZ-8 material survived a long cycling process, thereby retaining most of their original structural integrity. However, a partial deterioration can also be seen in the structural morphology of the nanosphere. In concern to a long and continuous charge–discharge process, such limited levels of structural depletion are expected in the electrode materials. This natural degradation might be a result of a continuous intercalation and deintercalation process during the ongoing electrochemical activity. Furthermore, a few FE-SEM images of the Ni@CCZ-8/NF electrode after the cycling process were measured at different locations that are presented in Fig. S10(a) and (b) of the ESI.† The FE-SEM images in Fig. S10(a)(i) and (b)(ii) of the ESI† showed the magnified view of a part of the Ni@CCZ-8/NF electrode surface after the cycling test. As the electrode was prepared by the binder coating process, the surface of the electrode contained the coated material along with the debris of additives such as PVDF and super-P carbon particles. Several Ni@CCZ-8 nanospheres can be seen amongst the additives from the binder slurry as shown in the magnified FE-SEM images in Fig. S10(a)(ii) and (b)(ii) of the ESI.† At a further magnification, Fig. S10(a)(iii) and (b)(iii) of the ESI† revealed the Ni@CCZ-8/NF nanospheres that seem to endure their physical morphology with minimal deterioration. The multilayered morphology may provide additional structural integrity in association with supportive mechanical stability, thus resulting in considerable cycling retention of 87.4%, even after 20 000 charge–discharge cycles. The EDS and elemental mapping of the Ni@CCZ-8 HCDSNS/NF electrode is given in Fig. S10(c) of the ESI,† which shows the Ni, Co, Cu, C, Zn, O, and N along with K. The presence of K element is a result of subjecting the material to a long cycling process in the presence of KOH electrolyte. Fig. S10(d)(i–viii) of the ESI† shows the elemental mappings of the corresponding elements on the electrode after the cycling test. The inset of Fig. 4(g) shows the electrochemical impedance spectroscopy (EIS) plots before and after the cycling test. The R_s and R_{ct} values before the cycling test were 0.43 and 0.5 Ω, respectively. The R_s and R_{ct} values after the cycling test were 0.8 and 0.87 Ω. The schematic in Fig. 4(h) shows the detailed architecture of the Ni@CCZ-8 HCDSNSs. These particles were primarily composed of three distinct layers, with each layer having a different morphology. The innermost layer of the sphere (hollow core) comprises a nanoparticle matrix. The spherical core has a hollow interior. This empty volume is occupied by the electrolyte, through which there can be increased interactions between the electrolyte and electrode material. In addition, it enhances the wettability. The intermediate layer (primary shell) was composed of accumulated nanocubes. This layer provides a rough surface that offers additional surface area for ion penetration and charge adsorption. The outermost layer (secondary shell) is composed of porous nanosheets agglomerated over the nanospheres. Being 2D structures, these nanosheets have a high surface area and structural stability. Owing to the orientation of these nanosheets, several hot spots were formed, which supported the electrochemical reactions by allowing charges to penetrate the nanospheres. Owing to the multiple layers and hollow internal core filled with the electrolyte, the Ni@CCZ-8 HCDSNSs resemble a planet with multiple layers.

The Ni@CCZ-8/NF electrode was used as the positive electrode, and AC/NF was utilized as the negative electrode to fabricate a pouch-type HSC. The mass balance between both the positive and negative electrodes was achieved by the mass balancing eqn (S5).† The fabrication process for the AC/NF electrode is described in the ESI.† The total mass of the device was 3.9 mg. The electrodes were placed facing each other, separated by a filter paper that acted as an ion-permeable membrane that permitted only ions to pass through it and avoided direct contact with the working material from the electrodes. A 2 M KOH aqueous solution was used as the ionic electrolyte. The device was packed in an aluminum-laminated pouch and heat-sealed to prevent leakage. An illustration of a pouch-type HSC device is shown in Fig. 5(a). A suitable potential window for smooth redox activity within the device was determined by analyzing the CV at a fixed scan rate (15 mV s^{-1}) and altering the potential windows from 0–1 V to 0–1.65 V. In this CV optimizing test in Fig. 5(b), until 1.55 V, the CV curve seemed to be in shape, but as the potential window exceeded 1.55 V, the CV shape started deforming, indicating improper functioning of the device. Similarly, a GCD optimizing test (Fig. 5(c)) was performed to confirm a suitable operating potential window for the HSC. At 3 mA cm^{-2}, the HSC device was subject to the GCD test under varying potential windows. The HSC appeared to perform normally until 1.55 V. But, after that, a deformity in the discharge curve could be observed. These tests confirm that the HSC operates safely within the potential range of 0 to 1.55 V. The general CV profiles are shown in Fig. 5(d), which were measured at various scan rates (5–50 mV s^{-1}) under the potential window of 0–1.55 V. The CV curves exhibited redox characteristics owing to the positive Ni@CCZ-8/NF electrode and double-layer storage characteristics owing to the negative AC/NF electrode. The CV curves indicate proportional behavior with increasing scan rate, implying good electrochemical response and reversibility. The GCD curves of the HSC (Fig. 5(e)) were taken at the current densities varying from 1.5 to 10 mA cm^{-2} under the potential window of 0–1.55 V. The discharge curves exhibited a slight curvature at the top and became linear at the bottom. This signifies that the GCD curves also illustrate hybrid behavior owing to the combined energy storage mechanisms. As shown in Fig. 5(f), the areal capacitance values were plotted based on the GCD profiles using eqn (S2) for the ESI.† The HSC exhibited a good areal capacitance of 302.9 mF cm^{-2} (77.67 F g^{-1}) at 1.5 mA cm^{-2}. In Fig. 5(g), the areal energy density (ED) and areal power density (PD) of the HSC were calculated using eqn (S3) and (S4) as mentioned in the ESI.† The maximum ED value was 100.77 μW h cm^{-2} (25.58 W h kg^{-1}) and the maximum PD value was 7500 μW cm^{-2}

Open Access Article. Published on 04 March 2025. Downloaded on 5/10/2026 4:48:14 PM.
This article is licensed under a Creative Commons Attribution-NonCommercial 3.0 Unported Licence.

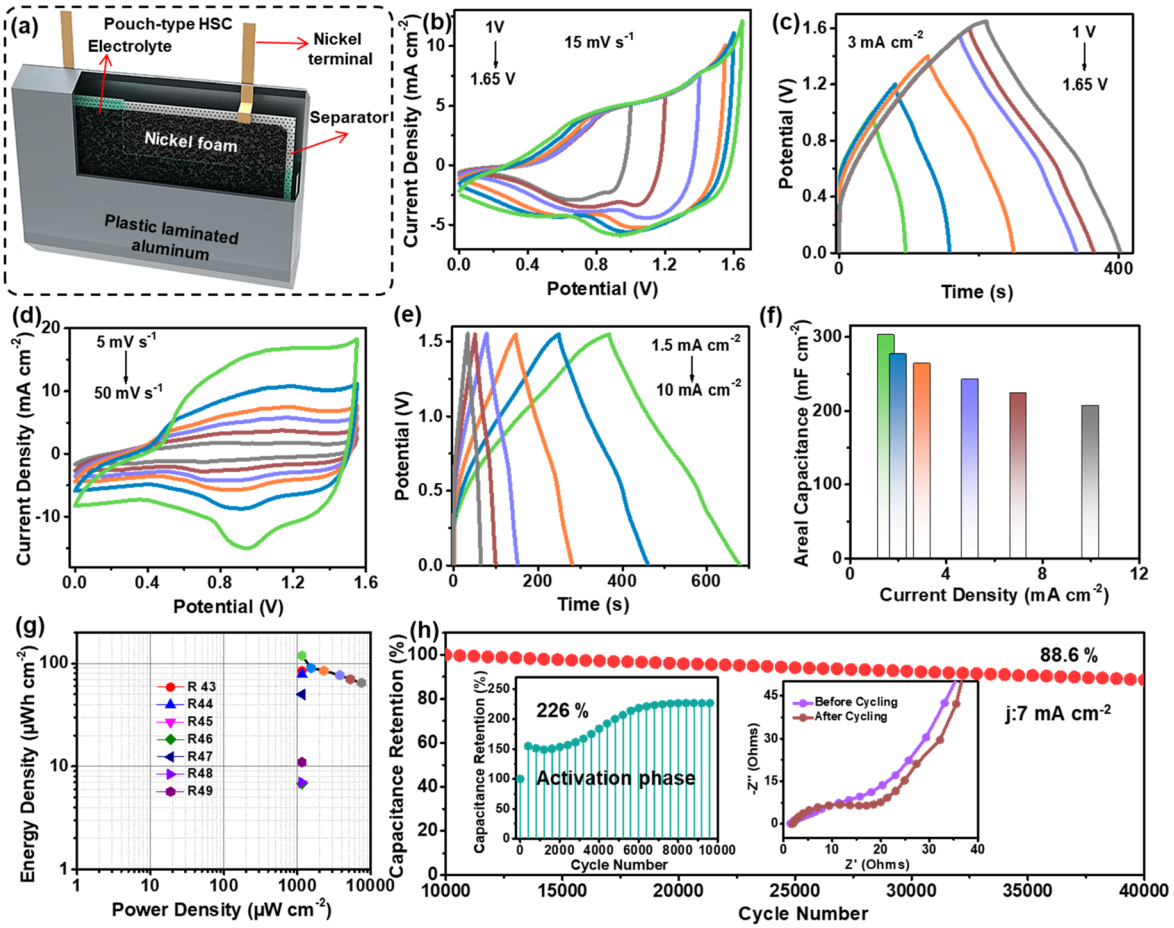

Fig. 5 (a) Schematic of the pouch-type HSC device. Potential window optimization of (b) CV curves and (c) GCD curves. (d) CV profiles, (e) GCD profiles, (f) areal capacitance values, (g) Ragone plot with comparative energy densities, and (h) cycling test result of the HSC device. Comparative Nyquist plots before and after the cycling test are shown in the inset of (h).

(25.58 W h kg^{-1}). The Ragone plot in Fig. 5(g) showed various energy densities compared with the previous literature. The comparison values of energy densities from previous literature are presented in Table 3. To verify its long-term sustainability, the HSC device was subjected to a cycling test with 40 000 charge/discharge cycles, as shown in Fig. 5(h). For the first 10 000 cycles, the device demonstrated an over-efficient capacitance retention of 226%, which is caused due to the activation of the working material present on the electrodes (in the inset of Fig. 5(h)). Nevertheless, from that point forth, the cycling process continued normally associated with slight fading. From 10 000 to 40 000 cycles, the device illustrated an 88.6% of capacitance retention. The EIS plots before and after cycling are shown in the inset of Fig. 5(h). The R_s and R_{ct} values before the cycling process were 1.47 and 5.09 Ω, whereas the R_s and R_{ct} values after the cycling process were 1.87 and 15.22 Ω, respectively. The variation in the charge transfer resistance might have been caused by a naturally degrading conductivity, as a result of multiple charge–discharges on high current density.

The as-fabricated HSC device was used as a power source to power several electronic devices, specifically to power radio-remote-operated electronic devices. The schematic in Fig. 6(a)

Table 3 Areal energy density comparison of the fabricated pouch-type HSC device with previously published devices

Positive electrode	Negative electrode	Electrolyte	Energy density	Ref.
NMS20 NFs	Activated carbon	1 M KOH	84.47 μW h cm^{-2}	44
NiCo LDH@Ag nanowires	Activated carbon	1 M KOH	78 μW h cm^{-2}	45
$Ti_3C_2T_x$	$Ti_3C_2T_x$	3 M H_2SO_4-PVA gel	0.32 μW h cm^{-2}	46
$NiCo_2O_4$ nanowires	Activated carbon	PVA-koh	6.8 μW h cm^{-2}	47
$Ni(OH)_2$NL@Cu_2O CAS	BDAC	1 M KOH	50 μW h cm^{-2}	48
Ni-Cu-Co LDH	Activated carbon	1 M KOH	7 μW h cm^{-2}	49
CW/PNC/PEDOT	CW/CMK-3	Polymer gel	11 μW h cm^{-2}	50
Ni@CCZ-8	Activated carbon	2 M KOH	100.77 μW h cm^{-2}	This work

 This journal is © The Royal Society of Chemistry 2025

Open Access Article. Published on 04 March 2025. Downloaded on 5/10/2026 4:48:14 PM.
This article is licensed under a Creative Commons Attribution-NonCommercial 3.0 Unported Licence.

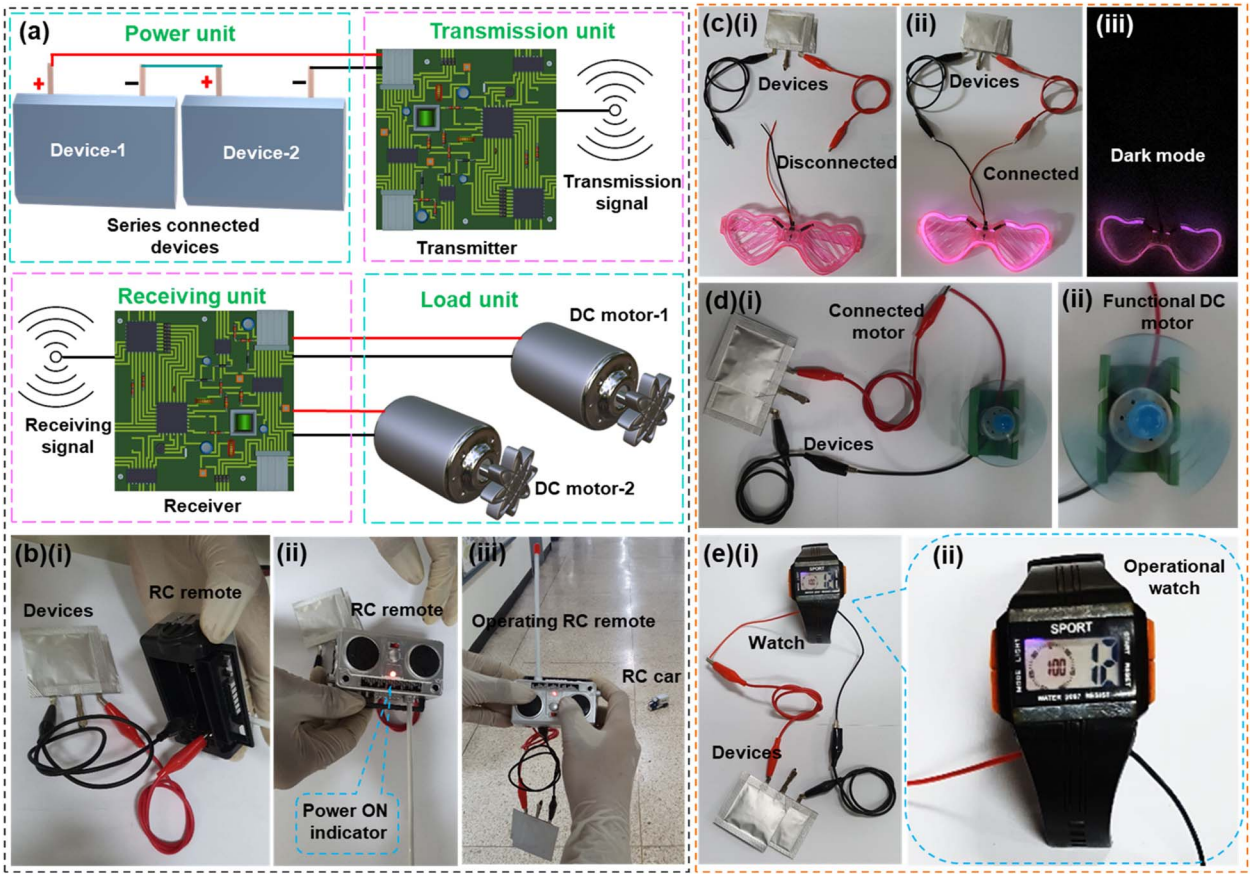

Fig. 6 (a) Schematic illustration of radio-controlled transmission and receiving of RC car, (b) (i–iii) photographic images of the remote controller powered by the HSC devices and operating RC car, (c) (i–iii) photographic images of the disconnected and connected conditions of LED goggles in daylight and darkness, (d) (i–iii) photographic images of the fully operational DC motor connected directly to the devices, and (e) (i, ii) photographic images of the digital watch powered by the as-fabricated HSC devices.

illustrates the vital application of the fabricated HSC devices. The schematics represent the remote control (RC) transmitter and receiver of the RC car. This serves the purpose of a prototype for real-time and commercially utilized RC applications. The HSC devices are connected in series to extend their voltage window from 1.5 to 3 V, which is sufficient to power the transmitter circuit present in the remote controller. As the button is pressed within the remote, the corresponding signal will be transmitted through it. On the other end, a receiver circuit that is integrated within the RC car gets the signal and triggers a control that engages the direct current (DC) motors (load). The receiver circuit and the motors are powered by the internal battery unit present in the RC car. Fig. 6(b)(i) shows the photographic image of the remote controller connected to the HSC devices and Fig. 6(b)(ii) shows the power indication in the remote. The photographic image in Fig. 6(b)(iii) displays the functioning of the remote that engages the functions within the controlled RC car. A live video is given in Video V1 of the ESI.† An open circuit containing the HSC and inactive light-emitting diode (LED) goggles is shown in Fig. 6(c)(i). Later, the same circuit is connected with the HSC devices, and the LED was observed to be in the active state as shown in Fig. 6(c)(ii) (daylight) and Fig. 6(c)(iii) (darkness). Furthermore, the devices were tested for their ability to support high-current appliances such as DC motors. In Fig. 6(d)(i) and (ii), the DC motor was observed to be powered effectively by the HSC devices, thus proving their ability to tolerate the high current-based electrical loads. The photographic images in Fig. 6(d)(ii) show a high-magnification image of the operating motor. Moreover, the devices were also tested for their capability to power the digital electronics such as a digital watch. The photographic images in Fig. 6(e)(i) show the digital watch connected to the HSC devices. The photographic image in Fig. 6(e)(ii) shows the function of the watch that displays time appropriately. Under fully charged conditions, the devices were able to power the watch for about 30 min per single charge. The operation of the watch powered by the HSC is shown in Video V2 of the ESI.† These applications prove that the as-fabricated materials and HSC devices are functional and reliable in real time.

4. Conclusion

In summary, 3D hierarchical CCZ HCDSNSs composed of multiple nanoarchitectures were synthesized *via* a facile solvothermal process. The as-synthesized Ni@CCZ-8/NF working electrode from its corresponding sample exhibited elevated electrochemical properties with an areal capacity of 124.46 μA h cm^{-2} (76.06 F g^{-1}) with a cycling efficiency of 87.4% at 7 mA

Open Access Article. Published on 04 March 2025. Downloaded on 5/10/2026 4:48:14 PM.
This article is licensed under a Creative Commons Attribution-NonCommercial 3.0 Unported Licence.

cm^{-2}. This positive electrode was paired with the AC/NF negative electrode to construct a pouch-type HSC device that showed the ED value of 100.77 μW h cm^{-2} as well as the PD value of 7500 μW cm^{-2} along with a good areal capacitance of 302.91 mF cm^{-2} (77.6 F g^{-1}). The device also revealed a considerable cycling efficiency of 88.6% over 40 000 cycles at 7 mA cm^{-2}. Furthermore, the as-fabricated HSC device can power radio-remote-operated electronics for practical applications. Therefore, the primary objective of exploring unique and complex multilayered morphologies in the field of energy storage was achieved. The synthesis process adopted to fabricate Ni@CCZ-8 HCDSNSs was facile, cost-effective, and tunable. Multi-layered hollow-cored nanospheres can be considered a suitable futuristic material to meet the ever-increasing energy demand.

Data availability

Data will be made available upon request from the authors.

Conflicts of interest

The authors declare that they have no known competing financial interests or personal relationships that could have appeared to influence the work reported in this paper.

Acknowledgements

This work was supported by the National Research Foundation of Korea (NRF) grant funded by the Korean government (MSIP) (No. 2018R1A6A1A03025708).

References

1 T. M. Gür, *Energy Environ. Sci.*, 2018, **11**, 2696–2767.
2 B. Ramulu, G. Nagaraju, S. C. Sekhar and J. S. Yu, *J. Alloys Compd.*, 2019, **772**, 925–932.
3 B. Ramulu, S. J. Arbaz, M. Nagaraju and J. S. Yu, *Nanoscale*, 2023, **15**, 13049–13061.
4 S. C. Sekhar, G. Nagaraju and J. S. Yu, *Nano Energy*, 2018, **48**, 81–92.
5 S. Chen, W. Xing, J. Duan, X. Hu and S. Z. Qiao, *J. Mater. Chem. A*, 2013, **1**, 2941–2954.
6 L. Mao, K. Zhang, H. S. O. Chan and J. Wu, *J. Mater. Chem.*, 2012, **22**, 1845–1851.
7 B. Ramulu and J. S. Yu, *Appl. Sci. Converg. Technol.*, 2024, **33**, 53–61.
8 D. Zhang, T. Wang, M. Zhang, Y. Miao, Q. Feng, X. Chen, Z. Hu, L. Ma, J. Qi and F. Wei, *J. Alloys Compd.*, 2022, **927**, 166974.
9 A. Toghan, M. Khairy, E. Kamar and M. Mousa, *J. Mater. Res. Technol.*, 2022, **19**, 3521–3535.
10 J. Sun, L. Guo, X. Sun, J. Zhang, L. Hou, L. Li, S. Yang and C. Yuan, *Batteries Supercaps*, 2019, **2**, 820–841.
11 G. Zhang, X. Xiao, B. Li, P. Gu, H. Xue and H. Pang, *J. Mater. Chem. A*, 2017, **5**, 8155–8186.
12 Q. Wei, F. Xiong, S. Tan, L. Huang, E. H. Lan, B. Dunn and L. Mai, *Adv. Mater.*, 2017, **29**, 1602300.
13 S. Zhai, H. E. Karahan, C. Wang, Z. Pei, L. Wei and Y. Chen, *Adv. Mater.*, 2020, **32**, 1902387.
14 S. J. Arbaz, S. C. Sekhar, B. Ramulu, M. Nagaraju and J. S. Yu, *Appl. Surf. Sci.*, 2022, **602**, 154288.
15 L. Lin, W. Lei, S. Zhang, Y. Liu, G. G. Wallace and J. Chen, *Energy Storage Mater.*, 2019, **19**, 408–423.
16 X. Gao, P. Wang, Z. Pan, J. P. Claverie and J. Wang, *ChemSusChem*, 2020, **13**, 1226–1254.
17 K. S. Kumar, N. Choudhary, Y. Jung and J. Thomas, *ACS Energy Lett.*, 2018, **3**, 482–495.
18 J. Cherusseri, D. Pandey and J. Thomas, *Batteries Supercaps*, 2020, **3**, 860–875.
19 L. Wang, H. Yang, T. Shu, X. Chen, Y. Huang and X. Hu, *ChemElectroChem*, 2017, **4**, 2428–2441.
20 B. Li, M. Yu, Z. Li, C. Yu, H. Wang and Q. Li, *Adv. Funct. Mater.*, 2022, **32**, 2201166.
21 M. Karuppaiah, X. Benadict Joseph, S.-F. Wang, B. Sriram, G. Antilen Jacob and G. Ravi, *Energy Fuels*, 2021, **35**, 12569–12580.
22 K.-C. Ho and L.-Y. Lin, *J. Mater. Chem. A*, 2019, **7**, 3516–3530.
23 C. V. M. Gopi, R. Vinodh, S. Sambasivam, I. M. Obaidat, R. M. N. Kalla and H.-J. Kim, *Mater. Today Energy*, 2019, **14**, 100358.
24 H. Zhao, Z. Zhang, C. Zhou and H. Zhang, *Appl. Surf. Sci.*, 2021, **541**, 148458.
25 K. Wang, Z. Shi, Y. Wang, Z. Ye, H. Xia, G. Liu and G. Qiao, *J. Alloys Compd.*, 2015, **624**, 85–93.
26 T. Bhat, S. Jadhav, S. Beknalkar, S. Patil and P. Patil, *Inorg. Chem. Commun.*, 2022, **141**, 109493.
27 Z. Wu, X. Pu, X. Ji, Y. Zhu, M. Jing, Q. Chen and F. Jiao, *Electrochim. Acta*, 2015, **174**, 238–245.
28 S. J. Arbaz, S. C. Sekhar, B. Ramulu and J. S. Yu, *Int. J. Energy Res.*, 2022, **46**, 4895–4907.
29 Y. He, L. Xie, S. Ding, Y. Long, X. Zhou, Q. Hu and D. Lin, *Dalton Trans.*, 2021, **50**, 4923–4931.
30 G. Saeed, S. Kumar, P. Bandyopadhyay, N. H. Kim and J. H. Lee, *J. Chem. Eng.*, 2019, **369**, 705–715.
31 Q. Zong, H. Yang, Q. Wang, Q. Zhang, Y. Zhu, H. Wang and Q. Shen, *J. Chem. Eng.*, 2019, **361**, 1–11.
32 T. Liu, L. Zhang, W. You and J. Yu, *Small*, 2018, **14**, 1702407.
33 S. J. Arbaz, B. Ramulu and J. S. Yu, *Appl. Surf. Sci.*, 2023, **635**, 157696.
34 N. A. Devi, S. Nongthombam, S. Sinha, R. Bhujel, S. Rai, W. I. Singh and B. P. Swain, *Diamond Relat. Mater.*, 2020, **104**, 107756.
35 Z. Li, L. Cao, P. Qin, X. Liu, Z. Chen, L. Wang, D. Pan and M. Wu, *Carbon*, 2018, **139**, 67–75.
36 A. S. Ahammad, N. Odhikari, S. S. Shah, M. M. Hasan, T. Islam, P. R. Pal, M. A. A. Qasem and M. A. Aziz, *Nanoscale Adv.*, 2019, **1**, 613–626.
37 B. Ramulu, G. Nagaraju, S. Chandra Sekhar, S. K. Hussain, D. Narsimulu and J. S. Yu, *ACS Appl. Mater. Interfaces*, 2019, **11**, 41245–41257.
38 F. Li, G. Li, H. Chen, J. Q. Jia, F. Dong, Y. B. Hu, Z. G. Shang and Y. X. Zhang, *J. Power Sources*, 2015, **296**, 86–91.
39 A. R. Mule, B. Ramulu and J. S. Yu, *Small*, 2022, **18**, 2105185.

 This journal is © The Royal Society of Chemistry 2025

Open Access Article. Published on 04 March 2025. Downloaded on 5/10/2026 4:48:14 PM.
This article is licensed under a Creative Commons Attribution-NonCommercial 3.0 Unported Licence.

40 H. Fang, L. Zhang, Y. Xing, S. Zhang and S. Wu, *Int. J. Electrochem. Sci.*, 2018, **13**, 8736–8744.
41 W. He, C. Wang, F. Zhuge, X. Deng, X. Xu and T. Zhai, *Nano Energy*, 2017, **35**, 242–250.
42 M. Sethi and D. K. Bhat, *J. Alloys Compd.*, 2019, **781**, 1013–1020.
43 X. Gao, Y. Zhang, M. Huang, F. Li, C. Hua, L. Yu and H. Zheng, *Ceram. Int.*, 2014, **40**, 15641–15646.
44 A. S. Kiran, B. Ramulu, S. J. Arbaz, M. Nagaraju, E. G. Shankar and J. S. Yu, *Appl. Surf. Sci.*, 2024, **645**, 158874.
45 S. C. Sekhar, G. Nagaraju and J. S. Yu, *Nano Energy*, 2017, **36**, 58–67.
46 C. J. Zhang, L. McKeon, M. P. Kremer, S.-H. Park, O. Ronan, A. Seral-Ascaso, S. Barwich, C. Ó. Coileáin, N. McEvoy and H. C. Nerl, in *MXenes*, Jenny Stanford Publishing, 2023, pp. 463–485.
47 L. Liu, Y. Feng, J. Liang, S. Li, B. Tian, W. Yao and W. Wu, *J. Power Sources*, 2019, **425**, 195–203.
48 S. C. Sekhar, G. Nagaraju, B. Ramulu and J. S. Yu, *Inorg. Chem. Front.*, 2019, **6**, 1707–1720.
49 S. C. Sekhar, G. Nagaraju, B. Ramulu, S. J. Arbaz, D. Narsimulu, S. K. Hussain and J. S. Yu, *Nano Energy*, 2020, **76**, 105016.
50 H. Yang, H. Xu, M. Li, L. Zhang, Y. Huang and X. Hu, *ACS Appl. Mater. Interfaces*, 2016, **8**, 1774–1779.